



Published in final edited form as:

*Magn Reson Med.* 2014 February ; 71(2): 477–485. doi:10.1002/mrm.25065.

## 3D Multislab, Multishot Acquisition for Fast, Whole-Brain MR Elastography with High SNR Efficiency

Curtis L Johnson<sup>1,2</sup>, Joseph L Holtrop<sup>2,3</sup>, Matthew DJ McGarry<sup>4</sup>, John B Weaver<sup>4,5</sup>, Keith D Paulsen<sup>4,6</sup>, John G Georgiadis<sup>1,2</sup>, and Bradley P Sutton<sup>2,3</sup>

<sup>1</sup>Department of Mechanical Science and Engineering, University of Illinois at Urbana-Champaign, Urbana, IL 61801

<sup>2</sup>Beckman Institute for Advanced Science and Technology, University of Illinois at Urbana-Champaign, Urbana, IL 61801

<sup>3</sup>Department of Bioengineering, University of Illinois at Urbana-Champaign, Urbana, IL 61801

<sup>4</sup>Thayer School of Engineering, Dartmouth College, Hanover, NH 03755

<sup>5</sup>Department of Radiology, Dartmouth-Hitchcock Medical Center, Lebanon, NH 03756

<sup>6</sup>Norris Cotton Cancer Center, Dartmouth-Hitchcock Medical Center, Lebanon, NH 03756

### Abstract

**Purpose**—To develop an acquisition scheme for generating magnetic resonance elastography (MRE) displacement data with whole-brain coverage, high spatial resolution, and adequate signal-to-noise ratio (SNR) in a short scan time.

**Theory and Methods**—A 3D multislab, multishot acquisition for whole-brain MRE with 2.0 mm isotropic spatial resolution is proposed. The multislab approach allowed for the use of short repetition time to achieve very high SNR efficiency. High SNR efficiency allowed for a reduced acquisition time of only six minutes while the minimum SNR needed for inversion was maintained.

**Results**—The mechanical property maps estimated from whole-brain displacement data with nonlinear inversion (NLI) demonstrated excellent agreement with neuroanatomical features, including the cerebellum and brainstem. A comparison with an equivalent 2D acquisition illustrated the improvement in SNR efficiency of the 3D multislab acquisition. The flexibility afforded by the high SNR efficiency allowed for higher resolution with a 1.6 mm isotropic voxel size, which generated higher estimates of brainstem stiffness compared with the 2.0 mm isotropic acquisition.

**Conclusions**—The acquisition presented allows for the capture of whole-brain MRE displacement data in a short scan time, and may be used to generate local mechanical property estimates of neuroanatomical features throughout the brain.

## INTRODUCTION

The application of magnetic resonance elastography (MRE) [1] in the study of the brain has received significant impetus in recent years from studies that indicate that the mechanical properties of brain parenchyma are very sensitive to neurological disease state [2–4]. Significant scientific and clinical interest in MRE exists due to the potential for distinguishing specific microstructural tissue characteristics through the mechanical properties [5], which is already demonstrating initial validation from animal models and histology [6–8]. While previous studies found success using global averages of brain tissue properties, recent technological developments focused on methods for improved local property estimation of specific neuroanatomical regions, including individual white matter tracts [9,10], lobes of the brain [11,12], and deep gray matter structures [13]. It stands to reason that measuring local properties in relevant brain regions may improve the sensitivity and specificity of MRE measures in the investigation of neurological conditions.

We previously presented a brain MRE imaging acquisition capable of capturing displacement data with increased spatial resolution, and demonstrated the improvement in estimating local mechanical properties with higher resolution [14]. While this acquisition produced repeatable estimates of the corpus callosum and corona radiata properties in the human brain [9], the imaging acquisition was limited to a small number of slices as in many other MRE studies [15–17]. Capturing full vector field shear wave propagation with high spatial resolution and signal-to-noise ratio (SNR) requires the collection of a significant amount of imaging data in a single experiment. The imaging coverage in the slice direction is often compromised to maintain an acceptable scan time, while studies pursuing whole-brain acquisitions have employed reduced spatial resolutions [2,18]. Taken together, the above discussion underlines the need for acquisition schemes capable of capturing whole-brain displacement data at high resolution to investigate the local mechanical properties of structures throughout large portions of the central nervous system.

This paper introduces a 3D multislabs, multishot acquisition for MRE with whole-brain imaging coverage and high spatial resolution [19]. The multislabs approach allows for improved SNR through high SNR efficiency, and has recently gained popularity in similar acquisitions such as in diffusion weighted imaging (DWI) [20–22], another imaging technique with traditionally long acquisition times. High SNR efficiency occurs through the balance of  $T_1$  signal recovery with the number of volume excitations, and typically occurs at a relatively short repetition time (TR) approximately 1.5x the tissue  $T_1$  value. The division of whole-brain coverage into multiple 3D volumes provides significant flexibility in TR and access to this balance to achieve high SNR efficiency with sufficient imaging coverage. This high efficiency ultimately enables data undersampling to reduce scan time while still maintaining adequate SNR for MRE.

We use the 3D multislabs, multishot MRE acquisition to generate whole-brain, full vector field displacement data with  $2.0 \times 2.0 \times 2.0$  mm<sup>3</sup> isotropic spatial resolution in just six minutes, which ultimately results in high quality mechanical property maps estimated with nonlinear inversion (NLI) [23,24]. Through a comparison with an equivalent 2D acquisition, we demonstrate the improved SNR afforded by the 3D multislabs approach as measured by

the octahedral shear strain-based SNR (OSS-SNR) [25]. Finally, we acquired a dataset with increased resolution ( $1.6 \times 1.6 \times 1.6 \text{ mm}^3$ ) that suggests spatial resolution has a large effect on parameter estimation in the brainstem.

## THEORY

### Imaging Coverage and SNR Efficiency

The traditional approach to MRI is to divide the total imaging volume into thin slices that are sampled with a 2D  $k$ -space. Since each slice can be excited sequentially in a single TR, this is often an expedient way to cover a large volume without much penalty in time. When larger coverage is needed the TR is generally made longer to accommodate the increased number of slices. This has the effect of increasing the total acquisition time, though without much increase in SNR as TR becomes much greater than the tissue  $T_1$ -relaxation value:

$$SNR_{T_1} \propto 1 - 2e^{-\frac{(TR-TE/2)}{T_1}} + e^{-\frac{TR}{T_1}} \quad (1)$$

In whole-brain acquisitions with high-resolution, where many slices are needed for full coverage, this approach often results in TRs as long as 10 seconds. Since the  $T_1$  of brain tissue is between 1 and 2 seconds, the extra time spent acquiring data with such a long TR provides minimal SNR benefit.

As an alternative to 2D slice sampling with long TRs, acquisitions can sample the entire volume with a 3D  $k$ -space. 3D sampling requires multiple excitations,  $N_{ex}$ , of the same imaging volume that contribute to the SNR of the acquisition by increasing the total readout time per volume:

$$SNR_{ex} \propto \sqrt{N_{ex}} \quad (2)$$

Unfortunately, large volumes for whole-brain coverage need many excitations to achieve high resolution in the slice direction, though the volume can only be excited once per TR. This approach is very slow as there is a significant waiting period in each TR after the necessary gradients and RF pulses are applied. Minimizing this downtime and overcoming the resulting long acquisition time requires a very short TR, which decreases acquisition SNR from lack of sufficient  $T_1$  recovery.

In the discussion of appropriate imaging volume and sampling strategy it is useful to formulate the tradeoffs in TR and  $N_{ex}$  in terms of SNR efficiency,  $\eta_{SNR}$ , defined as the ratio of SNR to the square root of total acquisition time equal to  $TR \cdot N_{ex}$  with the in-plane  $k$ -space trajectory fixed:

$$\eta_{SNR} \propto \frac{SNR_{T_1} \cdot SNR_{ex}}{\sqrt{TR \cdot N_{ex}}} \quad (3)$$

After substituting the expression from Eqs. (1) and (2) it becomes clear that TR, TE, and the tissue  $T_1$  value determine SNR efficiency:

$$\eta_{SNR} \propto \frac{1 - 2e^{-\frac{(TR-TE/2)}{T_1}} + e^{-\frac{TR}{T_1}}}{\sqrt{TR}} \quad (4)$$

Figure 1 plots the relative SNR efficiency as a function of TR for both white and gray matter using Eq. (4). For white matter and gray matter, which have  $T_1$  values at 3T of 1084 and 1820 ms [26], maximum SNR efficiency occurs with TRs of approximately 1500 and 2400 ms, respectively. These optimal TRs are calculated with a TE of 73 ms used in this work.

Maximizing SNR efficiency by choosing an optimal TR does not directly reduce the long scan times necessary for whole-brain coverage with high spatial resolution. However, the surplus of SNR afforded by the improved efficiency allows for the use of fewer motion encoding time points and incorporation of parallel imaging to reduce acquisition time while maintaining an adequate SNR for MRE inversion.

## METHODS

### 3D Multislab, Multishot Acquisition

The 3D multislab, multishot acquisition generates MRE data with whole-brain coverage by dividing the total imaging volume into multislice slabs. Each slab of an image is excited sequentially so that a single  $k$ -space shot is acquired for each volume in a single TR, and multiple TRs are used to achieve the desired multishot  $k$ -space sampling. The reduced number of imaging volumes allows for the use of a short TR and thus high SNR efficiency. A stack-of-spirals trajectory samples the 3D  $k$ -space of each slab, with spiral shots distributed in-plane ( $k_x, k_y$ ) and blipped encoding in  $k_z$ . Multiple interleaved  $k$ -space shots reduce field inhomogeneity distortions and  $T_2^*$ -induced blurring through short readout durations. Figure 2 displays the pulse sequence diagram where motion-encoding gradients are applied on either side of the refocusing pulse and a single  $k$ -space shot is acquired in each excitation. Gradient blips played before the in-plane readouts define the sampled  $k_z$  plane. The total number of excitations per volume is equal to the number of acquired in-plane  $k$ -space shots times the number of slices per slab.

The specific implementation of the 3D multislab, multishot acquisition employed here uses ten slabs of eight 2.0 mm thick slices and TR/TE = 1800/73 ms. Slabs are interleaved and overlapped by 25% to reduce slab boundary artifacts, with overlapped slices discarded, resulting in 120 mm of total coverage in the superior-inferior direction. The 120×120 in-plane matrix fills a square field-of-view of 240 mm with 2.0×2.0×2.0 mm<sup>3</sup> isotropic voxel size. In-plane  $k$ -space sampling used a single 20 ms constant-density spiral trajectory ( $R = 3$ ) [27]. The number and size of slabs were chosen with considerations of coverage of key brain structures, SNR efficiency for white and gray matter, total scan time, and necessary timing of each excitation block for compatibility with MRE encoding.

## Motion-Induced Phase Error Correction

We previously demonstrated that multishot MRE acquisitions need correction for motion-induced phase error caused by shot-to-shot variations in acquired phase [14]. These errors result from rigid body motions due to inconsistencies in the applied motion, and include bulk phase differences and  $k$ -space trajectory shifts that cause signal loss and artifacts when shots are combined during image reconstruction. Acquisitions that utilize shots distributed throughout a 3D  $k$ -space need an appropriate navigator acquisition to correct for trajectory shifts in  $k_x$ ,  $k_y$ , and  $k_z$  [28]. The proposed imaging sequence includes acquisition of the navigator volume as a low-resolution, single-shot 3D stack-of-spirals after a second refocusing pulse at an echo time of 130 ms [21] (Figure 2). Each navigator covers the slab field-of-view with a  $15 \times 15 \times 8$  matrix for a resolution of  $16.0 \times 16.0 \times 2.0$  mm<sup>3</sup>.

Correction of motion-induced phase errors in multishot DWI applications typically involves estimation of phase offsets and trajectory shifts relative to a reference navigator with no encoding applied. However, this technique typically removes all low-resolution imaging phase. In MRE, the desired displacement signal is encoded in the image phase and hence, standard DWI correction may remove part of the useful MRE signal. In this work, our implementation of phase error correction for multishot MRE uses the average of all navigators acquired for a volume as the reference for that volume. The number of navigators for each volume is equal to the number of excitations, and the average preserves the desired “true” phase. Phase offsets and trajectory shifts are calculated using maximum likelihood estimation [28] relative to this averaged reference.

## Human Brain MRE Data

We acquired MRE displacement data on three healthy subjects (male; 26–28 years old) to demonstrate the performance of the proposed 3D multishot, multislab sequence. Scanning used a Siemens 3T TIM Trio MRI scanner (Siemens Medical Solutions; Erlangen, Germany) with a 12-channel head coil. Our Institutional Review Board approved the study and all subjects provided written, informed consent.

The 3D multislab, multishot pulse sequence includes flow-compensated gradients to encode 50 Hz displacements in the brain generated with a remote actuation system [14]. Imaging is repeated to encode motion along each of the three gradient axes separately, with both positive and negative polarities, and at four time points spaced over a single vibration period. The acquisition generates full vector field, complex displacement data at  $2.0 \times 2.0 \times 2.0$  mm<sup>3</sup> isotropic spatial resolution in a total scan time of six minutes.

To demonstrate the improvement in SNR efficiency, we acquired an additional dataset using an equivalent 2D sampling scheme on one subject in the same imaging session as a 3D multislab acquisition. 60 slices of 2.0 mm thickness generated the same field-of-view and 120 mm coverage and required a TR of 10800 ms. In-plane  $k$ -space sampling used the same spiral trajectory and reduction factor ( $R = 3$ ), and all other imaging parameters remained the same as in the 3D multislab acquisition, though the navigator was equivalently acquired in 2D. Since the 2D acquisition has the same in-plane sampling scheme as the 3D multislab acquisition, the total scan times should also be equal. However, because there is no overlap

of slabs, and thus no acquired data that needs to be discarded, the total 2D acquisition time is slightly shorter at 4 min 30 s.

Finally, we used the 3D multislabs, multishot sequence to acquire a dataset at higher spatial resolution on one subject for comparison with results from 2.0 mm displacement data. We used an increased 150×150 in-plane matrix size on the 240 mm field-of-view, along with 1.6 mm thick slices, for an isotropic 1.6×1.6×1.6 mm<sup>3</sup> spatial resolution. The higher in-plane resolution required longer data sampling times, and two spiral interleaves ( $R = 2$ ) were used to maintain a 20 ms readout duration. All other imaging parameters were the same, including TE and TR, and the total acquisition time was 11 min 45 s.

Iterative image reconstruction of each dataset was performed using IMPATIENT on graphics processing units (GPUs) [29,30]. Reconstruction incorporated phase offsets and  $k$ -space trajectory shifts for motion correction, sensitivity encoding (SENSE) [31], and field inhomogeneity correction [32] with an independently acquired fieldmap [33]. The NLI algorithm [23,24] estimated the viscoelastic storage and loss moduli,  $G'$  and  $G''$ , from each displacement dataset.

### Segmentation Analysis

The imaging protocol also included a high-resolution  $T_1$ -weighted MPRAGE acquisition (1.0×1.0×1.0 mm<sup>3</sup>; TR/TI/TE = 1900/900/2.3 ms) and  $T_2$ -weighted acquisition (2.0×2.0×2.0 mm<sup>3</sup>; TR/TE = 10500/93 ms) co-registered with the MRE dataset. All segmentation analysis used the  $T_1$ -weighted data in FSL [34] with the MNI structural atlas [35] and Harvard-Oxford structural atlas [36] following a procedure outlined previously [9]. Masks were created for investigating white and cortical gray matter (WM and GM) of the cerebrum and cerebellum, as well as the brainstem.

## RESULTS

The 3D multislabs, multishot acquisition generated whole-brain displacement data with high SNR, as characterized by the octahedral shear strain-based SNR measure (OSS-SNR) [25]. The average OSS-SNR of the three datasets acquired is 4.19, with every dataset above the minimum of 3.0 needed for inversion [25]. Generating high quality MRE data with a multishot acquisition also required correction for motion-induced phase errors. Figure 3.A provides an example of phase from data reconstructed without phase error correction. Clearly visible are increased noise and disjointed phase from slab-to-slab, which indicates phase artifacts present in the individually reconstructed slabs. Figure 3.B presents the same data with motion-induced phase error correction included in the reconstruction and shows smooth phase with a clear increase in SNR.

Whole-brain mechanical property maps appear to agree well with neuroanatomy. Figure 4 presents the storage and loss modulus from one subject, along with the corresponding  $T_2$ -weighted anatomical images. Regions of cerebrospinal fluid appear as soft tissue, as expected, including cortical sulci and the lateral and fourth ventricles. Also visible in Figure 4.B are the cerebellum and brainstem appearing as soft and stiff, respectively. The apparent trend across the three volunteers of a relatively soft cerebellum agrees with previous reports

of cerebellar properties from MRE [12,37]. The apparent elevated stiffness of the brainstem is also expected given its tight, highly aligned fiber structure [38,39]. The loss modulus map exhibits less contrast than in the storage modulus, though regions of cerebrospinal fluid are similarly visible. Regions near the *falx cerebri* and *tentorium cerebelli*, which are hard dura matter membranes, appear as areas of low loss modulus that may be influenced by the wave behavior at these interfaces [17].

Figure 5 presents displacement fields and property maps from the same slice of data acquired in 2D and 3D on the same subject. Both datasets are acquired in the same imaging session with an identically prescribed field-of-view and are expected to be co-registered, which is verified by the magnitude images of Figures 5.A–B. The displacement data shows nearly identical deformation patterns between acquisitions, though the 2D acquisition resulted in decreased SNR. The OSS-SNR of the 2D dataset is 2.52, which is below the minimum needed for inversion [25], while the OSS-SNR of the 3D dataset is 3.84. Figures 5.E–H present the storage and loss moduli estimated from the two acquisitions with NLI, with the 2D data resulting in poor property maps due to low OSS-SNR.

Table 1 collects the average storage and loss moduli of the cerebrum, cerebellum, and brainstem of the same subject assessed with both 1.6 and 2.0 mm spatial resolutions, for comparison. The 1.6 mm acquisition produced property estimates of cerebral WM and GM that are very similar to those from the 2.0 mm acquisition, and the same is true of cerebellar WM and GM properties. On the other hand, the 1.6 mm acquisition returned an estimated  $G'$  for the brainstem that is higher than estimated with the lower resolution (3.57 vs. 3.01 kPa), and a  $G''$  that is lower (1.11 vs. 1.28 kPa). Figure 6 presents co-registered storage modulus estimates from both resolutions demonstrating the similar cerebellar profiles and differences in the brainstem.

The effect sizes for each comparison were calculated using Cohen's  $d$  with pooled variance [40] and are presented in Table 1, as well. Effect size is used here to evaluate the magnitude of the difference in properties as a function of spatial resolution. The differences in brainstem properties with resolution were the only comparisons with a large effect size ( $\geq 0.8$ ), while all other comparisons had very small effect sizes ( $< 0.2$ ).

## DISCUSSION

The 3D multislabs, multishot acquisition scheme captures MRE displacement data by using multiple 3D volumes that cover the entire brain. The small number of imaging volumes does not require a long TR, and thus high SNR efficiency can be achieved. This high SNR efficiency allows for the reduction of total acquisition time while maintaining adequate SNR necessary for inversion. Scan time was reduced by undersampling in both  $k$ -space and MRE time domains. The use of parallel imaging reduced the acquisition time by a factor of 3 and the SNR by a factor of  $\sqrt{3}$ , along with a  $g$ -factor penalty based on the object and receiver coil geometries [41]. Additionally, only four samples of the vibration are captured, as opposed to the typical eight of most MRE acquisitions. This halves the total acquisition time, but also reduces the OSS-SNR by a factor of  $\sqrt{2}$  [25]. Despite the reduced acquisition time, the 3D multislabs, multishot sequence generated whole-brain MRE datasets with

adequate OSS-SNR. The total acquisition time of six minutes makes this the fastest MRE acquisition that generates whole-brain, full vector field displacements with  $2.0 \times 2.0 \times 2.0$  mm<sup>3</sup> isotropic spatial resolution, to our knowledge. Note that the high SNR efficiency of the 3D multislabs, multishot acquisition is based on acquisition parameters, while the OSS-SNR measure also depends on factors not focused on in the paper. These include amplitude and frequency of vibration, subject-specific tissue properties, and characteristics of the MRE encoding gradient waveforms.

Motion-induced phase errors lead to signal cancellation and artifacts in multishot acquisitions, and require a correction procedure to recover SNR and minimize artifacts in the phase images. Correcting the slab-to-slab phase inconsistencies is especially critical in MRE where the underlying tissue properties are estimated from spatial variations in phase. Without proper correction, this type of phase artifact will cause errors in estimated properties on either side of the slab boundary and require spatial filtering [18], thus reducing the spatial resolution of the property maps.

We previously suggested that the source of rigid body motion error in brain MRE is imperfections in applied harmonic motion amplitude from the actuation system [14]. Recently, Engström and Skare demonstrated that  $k_z$  trajectory shifts occurring in multislabs DWI acquisitions are very small and do not require correction [22]. However, actuation in brain MRE directly causes head rotations about the magnet  $x$ -axis and any amplitude variations will generate  $k_z$  errors in the presence of  $y$ -gradients that require correction [42,43]. Additional sources of rigid body motion include microscopic subject movement or scanner table vibrations induced by gradient switching [44]. Note that the correction technique presented here accounts only for phase errors induced by rigid body motion. Residual phase errors due to brain motion during cardiac pulsation [45] or shear displacement fields from off-frequency vibrations [46] may persist.

Also note that there is no perceptible “venetian blind” artifact between slabs in Figure 3.B. The artifact arises from imperfect RF pulse profiles that cause signal loss at the edges of neighboring slabs [47], and the magnitude images associated with the data in Figure 3 do show this artifact. The reduced magnitude signal at the slab edges should translate to increased phase variance and lower phase SNR, though this is not significant enough to affect the phase images or OSS-SNR calculation. Any additional background phase field associated with the RF pulse profiles is removed during subtraction of images with opposite encoding polarities.

The improvement in SNR efficiency of the 3D multislabs, multishot acquisition is demonstrated by the comparison with the equivalent 2D acquisition in Figure 5. Based on the relationship in Eq. 4 we expect the 3D acquisition to have 2.25x the SNR of the 2D acquisition in WM and 1.74x in GM. However, the 3D dataset only has a 1.52x improvement in OSS-SNR as averaged over the entire brain. This discrepancy between theoretical and experimental results likely stems from the residual phase error caused by non-rigid body motion, as mentioned above. Since the equivalent 2D acquisition in this case is actually a single-shot sequence it is not subject to the signal loss that results from phase errors in multishot sequences. Thus, any additional SNR loss caused by this residual phase



error in the 3D multislabs, multishot acquisition will decrease the observed SNR margin. Nonetheless, the 2D acquisition used here still has SNR too low for accurate inversion. Note that in practice, a multishot approach would be needed for the 2D acquisition by removing the benefit of parallel imaging to improve the SNR at the expense of increased scan time by at least a factor of 2.

Figures 5.E–H highlight the importance of maintaining an adequate SNR level in MRE. The excessive noise in the 2D data leads to model/data mismatch during inversion that corrupts the resulting mechanical property maps. The fine features of Figure 5.F, including the lateral ventricles, are almost completely lost in the 2D results of Figure 5.E. The loss modulus results (Figures 5.G–H) also demonstrate the obscuring of fine ventricle features and lower values along the brain midline. This comparison further reinforces the argument that 3D multislabs sampling schemes are superior to their equivalent 2D counterparts in applications requiring whole-brain imaging coverage.

The high SNR efficiency of the 3D multislabs approach also affords significant flexibility for developing acquisitions with greater spatial resolution in specific applications. We tested the limits of the 3D acquisition by increasing the spatial resolution to  $1.6 \times 1.6 \times 1.6 \text{ mm}^3$ . This voxel size has a volume approximately half that of the 2.0 mm acquisition and should reduce the SNR by a factor of two. This loss was partially offset by the longer readout times necessitated by higher in-plane resolution and a parallel imaging factor of only  $R = 2$ . The resulting OSS-SNR of the dataset was 3.07, which is still above the minimum of 3.0 needed for inversion.

In general, the higher resolution generated slightly greater contrast in mechanical properties between WM and GM for both the cerebrum and cerebellum. This is expected given the very thin cortical structure, though the differences across resolution are small and within the measurement uncertainty reported previously for 2.0 mm spatial resolution [9]. However, the brainstem, which is a very stiff, sharply delineated structure, appears as having higher  $G'$  and lower  $G''$  at the higher spatial resolution. This is likely due to the need for higher resolution data to avoid smoothing over the structure and underestimating its stiffness [14]. The difference in estimated brainstem properties could also be related to the different OSS-SNR level between acquisitions, though the similarity in cerebellar properties and profiles in Table 1 and Figure 6 indicate strong agreement between the two datasets. Future work will look to quantify the material properties of the healthy brainstem, their repeatability, and the effect of MRE spatial resolution.

## CONCLUSIONS

While the implementation of MRE acquisitions with improved spatial resolution allows the measurement of local mechanical properties in the human brain, acquiring high quality MRE displacement data over the entire brain in a short scan time remains challenging. In this paper, we introduce a novel acquisition scheme for brain MRE based on 3D multislabs, multishot imaging. This approach is designed to maximize SNR efficiency by using an optimal TR based on the tissue relaxation times. Incorporation of time reduction methods through parallel imaging ultimately resulted in an acquisition capable of capturing whole-

brain displacement data with 2.0 mm isotropic spatial resolution in just six minutes while maintaining adequate SNR for inversion. This acquisition allows the probing of local neuroanatomical regions across the brain including the entire length of the corticospinal tracts, the four lobes of the brain and the cerebellum, and deep white and gray matter structures. The SNR efficiency also provides flexibility through tradeoffs in acquisition parameters to develop targeted acquisitions at even higher resolution for specific applications. By increasing the resolution to a 1.6 mm isotropic voxel size, we obtained an apparently improved estimate of the brainstem stiffness. The above results suggest that future progress in brain MRE is associated with gains in spatial resolution.

## Acknowledgments

The Biomedical Imaging Center of the Beckman Institute for Advanced Science and Technology and the Richard W. Kritzer Fund at the University of Illinois at Urbana-Champaign provided support for this work, while the Beckman Graduate Fellows Program of the Beckman Institute provided support for CLJ. NIH/NIBIB grant R21-EB009768 supported development of the IMPATIENT reconstruction and grant R01-EB004632 supported development of the nonlinear inversion algorithm.

## References

1. Muthupillai R, Lomas DJ, Rossman PJ, Greenleaf JF, Manduca A, Ehman RL. Magnetic Resonance Elastography by Direct Visualization of Propagating Acoustic Strain Waves. *Science*. 1995; 269:1854–1857. [PubMed: 7569924]
2. Murphy MC, Huston J, Jack CR, Glaser KJ, Manduca A, Felmlee JP, Ehman RL. Decreased Brain Stiffness in Alzheimer's Disease Determined by Magnetic Resonance Elastography. *J Magn Reson Imaging*. 2011; 34:494–498. [PubMed: 21751286]
3. Streitberger K-J, Sack I, Krefting D, Pfüller C, Braun J, Paul F, Wuerfel J. Brain Viscoelasticity Alteration in Chronic-Progressive Multiple Sclerosis. *PLoS One*. 2012; 7:e29888. [PubMed: 22276134]
4. Freimann FB, Streitberger K-J, Klatt D, Lin K, McLaughlin JR, Braun J, Sprung C, Sack I. Alteration of Brain Viscoelasticity After Shunt Treatment in Normal Pressure Hydrocephalus. *Neuroradiology*. 2012; 54:189–196. [PubMed: 21538046]
5. Sack I, Jöhrens K, Wuerfel J, Braun J. Structure-Sensitive Elastography: on the Viscoelastic Powerlaw Behavior of in Vivo Human Tissue in Health and Disease. *Soft Matter*. 2013; 9:5672–5680.
6. Schregel K, Wuerfel E, Garteiser P, Gemeinhardt I, Prozorovski T, Aktas O, Merz H, Petersen D, Wuerfel J, Sinkus R. Demyelination Reduces Brain Parenchymal Stiffness Quantified in Vivo by Magnetic Resonance Elastography. *P Natl Acad Sci USA*. 2012; 109:6650–6655.
7. Riek K, Millward JM, Hamann I, Mueller S, Pfueller CF, Paul F, Braun J, Infante-Duarte C, Sack I. Magnetic Resonance Elastography Reveals Altered Brain Viscoelasticity in Experimental Autoimmune Encephalomyelitis. *NeuroImage Clin*. 2012; 1:81–90. [PubMed: 24179740]
8. Freimann FB, Müller S, Streitberger K-J, Guo J, Rot S, Ghori A, Vajkoczy P, Reiter R, Sack I, Braun J. MR Elastography in a Murine Stroke Model Reveals Correlation of Macroscopic Viscoelastic Properties of the Brain with Neuronal Density. *NMR Biomed*. 2013; 26:1534–1539. [PubMed: 23784982]
9. Johnson CL, McGarry MDJ, Gharibans AA, Weaver JB, Paulsen KD, Wang H, Olivero WC, Sutton BP, Georgiadis JG. Local Mechanical Properties of White Matter Structures in the Human Brain. *NeuroImage*. 2013; 79:145–152. [PubMed: 23644001]
10. Romano AJ, Scheel M, Hirsch S, Braun J, Sack I. In Vivo Waveguide Elastography of White Matter Tracts in the Human Brain. *Magn Reson Med*. 2012; 68:1410–1422. [PubMed: 22252792]
11. McGarry MDJ, Johnson CL, Sutton BP, Van Houten EEW, Georgiadis JG, Weaver JB, Paulsen KD. Including Spatial Information in Nonlinear Inversion MR Elastography Using Soft Prior Regularization. *IEEE T Med Imaging*. 2013; 32:1901–1909.

12. Murphy, MC.; Huston, J.; Jack, CR.; Glaser, KJ.; Senjem, ML.; Chen, J.; Manduca, A.; Felmlee, JP.; Ehman, RL. Measuring the characteristic topography of brain stiffness with magnetic resonance elastography. Proceedings of the 21st Annual Meeting of ISMRM; Salt Lake City, Utah, USA. 2013. p. 2422
13. Guo J, Hirsch S, Fehlner A, Papazoglou S, Scheel M, Braun J, Sack I. Towards an Elastographic Atlas of Brain Anatomy. PLoS One. 2013; 8:e71807. [PubMed: 23977148]
14. Johnson CL, McGarry MDJ, Van Houten EEW, Weaver JB, Paulsen KD, Sutton BP, Georgiadis JG. Magnetic Resonance Elastography of the Brain Using Multishot Spiral Readouts with Self-Navigated Motion Correction. Magn Reson Med. 2013; 70:404–412. [PubMed: 23001771]
15. Green MA, Bilston LE, Sinkus R. In Vivo Brain Viscoelastic Properties Measured by Magnetic Resonance Elastography. NMR Biomed. 2008; 21:755–764. [PubMed: 18457350]
16. Sack I, Beierbach B, Wuerfel J, Klatt D, Hamhaber U, Papazoglou S, Martus P, Braun J. The Impact of Aging and Gender on Brain Viscoelasticity. NeuroImage. 2009; 46:652–657. [PubMed: 19281851]
17. Clayton EH, Genin GM, Bayly PV. Transmission, Attenuation and Reflection of Shear Waves in the Human Brain. J R Soc Interface. 2012; 9:2899–2910. [PubMed: 22675163]
18. Murphy MC, Huston J, Glaser KJ, Manduca A, Meyer FB, Lanzino G, Morris JM, Felmlee JP, Ehman RL. Preoperative Assessment of Meningioma Stiffness Using Magnetic Resonance Elastography. J Neurosurg. 2013; 118:643–648. [PubMed: 23082888]
19. Johnson, CL.; Holtrop, JL.; McGarry, MDJ.; Weaver, JB.; Paulsen, KD.; Sutton, BP.; Georgiadis, JG. Fast, Whole-Brain MR Elastography using a 3D Multislab Acquisition. Proceedings of the 21st Annual Meeting of ISMRM; Salt Lake City, Utah, USA. 2013. p. 2442
20. Van, AT.; Karampinos, DC.; Sutton, BP. High Resolution 3D Multi-slab Multi-shot Spin Echo Diffusion-Weighted Imaging. Proceedings of the 18th Annual Meeting of ISMRM; Stockholm, Sweden. 2010. p. 1618
21. Holtrop, JL.; Van, AT.; Sutton, BP. Pushing the Resolution of 3D Spin Echo Diffusion Acquisition. Proceedings of the 20th Annual Meeting of ISMRM; Melbourne, Australia. 2012. p. 1881
22. Engström M, Skare S. Diffusion-Weighted 3D Multislab Echo Planar Imaging for High Signal-to-Noise Ratio Efficiency and Isotropic Image Resolution. Magn Reson Med. 2013; 1002/mrm. 24594
23. Van Houten EEW, Miga MI, Weaver JB, Kennedy FE, Paulsen KD. Three-Dimensional Subzone-Based Reconstruction Algorithm for MR Elastography. Magn Reson Med. 2001; 45:827–837. [PubMed: 11323809]
24. McGarry MDJ, Van Houten EEW, Johnson CL, Georgiadis JG, Sutton BP, Weaver JB, Paulsen KD. Multiresolution MR Elastography Using Nonlinear Inversion. Med Phys. 2012; 39:6388–6396. [PubMed: 23039674]
25. McGarry MDJ, Van Houten EEW, Perriñez PR, Pattison AJ, Weaver JB, Paulsen KD. An Octahedral Shear Strain-Based Measure of SNR for 3D MR Elastography. Phys Med Biol. 2011; 56:N153–N164. [PubMed: 21654044]
26. Stanisz GJ, Odrobina EE, Pun J, Escaravage M, Graham SJ, Bronskill MJ, Henkelman RM. T1, T2 Relaxation and Magnetization Transfer in Tissue at 3T. Magn Reson Med. 2005; 54:507–512. [PubMed: 16086319]
27. Glover GH. Simple Analytic Spiral K-Space Algorithm. Magn Reson Med. 1999; 42:412–415. [PubMed: 10440968]
28. Van AT, Hernando D, Sutton BP. Motion-Induced Phase Error Estimation and Correction in 3D Diffusion Tensor Imaging. IEEE T Med Imaging. 2011; 30:1933–1940.
29. Stone SS, Haldar JP, Tsao SC, Hwu W-MW, Sutton BP, Liang Z-P. Accelerating Advanced MRI Reconstructions on GPUs. J Parallel Distr Com. 2008; 68:1307–1318.
30. Gai J, Obeid N, Holtrop JL, Wu X-L, Lam F, Fu M, Haldar JP, Hwu W-MW, Liang Z-P, Sutton BP. More IMPATIENT: a Gridding-Accelerated Toeplitz-Based Strategy for Non-Cartesian High-Resolution 3D MRI on GPUs. J Parallel Distr Com. 2013; 73:686–697.
31. Pruessmann KP, Weiger M, Börner P, Boesiger P. Advances in Sensitivity Encoding with Arbitrary K-Space Trajectories. Magn Reson Med. 2001; 46:638–651. [PubMed: 11590639]

32. Sutton BP, Noll DC, Fessler JA. Fast, Iterative Image Reconstruction for MRI in the Presence of Field Inhomogeneities. *IEEE T Med Imaging*. 2003; 22:178–188.
33. Funai AK, Fessler JA, Yeo DTB, Olafsson VT, Noll DC. Regularized Field Map Estimation in MRI. *IEEE T Med Imaging*. 2008; 27:1484–1494.
34. Jenkinson M, Beckmann CF, Behrens TEJ, Woolrich MW, Smith SM. *Fsl. NeuroImage*. 2012; 62:782–790. [PubMed: 21979382]
35. Mazziotta J, Toga AW, Evans A, Fox P, Lancaster J, Zilles K, Woods R, Paus T, Simpson G, Pike B, Holmes C, Collins L, Thompson PM, MacDonald D, Iacoboni M, Schormann T, Amunts K, Palomero-Gallagher N, Geyer S, Parsons L, Narr K, Kabani N, Le Goualher G, Boomsma D, Cannon T, Kawashima R, Mazoyer B. A Probabilistic Atlas and Reference System for the Human Brain: International Consortium for Brain Mapping (ICBM). *Philos T R Soc B*. 2001; 356:1293–1322.
36. Desikan RS, Segonne F, Fischl B, Quinn BT, Dickerson BC, Blacker D, Buckner RL, Dale AM, Maguire RP, Hyman BT, Albert MS, Killiany RJ. An Automated Labeling System for Subdividing the Human Cerebral Cortex on MRI Scans Into Gyral Based Regions of Interest. *NeuroImage*. 2006; 31:968–980. [PubMed: 16530430]
37. Zhang J, Green MA, Sinkus R, Bilston LE. Viscoelastic Properties of Human Cerebellum Using Magnetic Resonance Elastography. *J Biomech*. 2011; 44:1909–1913. [PubMed: 21565346]
38. Arbogast KB, Margulies SS. Material Characterization of the Brainstem From Oscillatory Shear Tests. *J Biomech*. 1998; 31:801–807. [PubMed: 9802780]
39. Arbogast KB, Margulies SS. A Fiber-Reinforced Composite Model of the Viscoelastic Behavior of the Brainstem in Shear. *J Biomech*. 1999; 32:865–870. [PubMed: 10433430]
40. Cohen, J. *Statistical Power Analysis for the Behavioral Sciences*. Lawrence Erlbaum Associates; 1988.
41. Pruessmann KP, Weiger M, Scheidegger MB, Boesiger P. SENSE: Sensitivity Encoding for Fast MRI. *Magn Reson Med*. 1999; 42:952–962. [PubMed: 10542355]
42. Anderson AW, Gore JC. Analysis and Correction of Motion Artifacts in Diffusion Weighted Imaging. *Magn Reson Med*. 1994; 32:379–387. [PubMed: 7984070]
43. Van AT, Karampinos DC, Georgiadis JG, Sutton BP. K-Space and Image-Space Combination for Motion-Induced Phase-Error Correction in Self-Navigated Multicoil Multishot DWI. *IEEE T Med Imaging*. 2009; 28:1770–1780.
44. Gallichan D, Robson MD, Bartsch A, Miller KL. TREMR: Table-Resonance Elastography with MR. *Magn Reson Med*. 2009; 62:815–821. [PubMed: 19585596]
45. O'Halloran RL, Holdsworth SJ, Aksoy M, Bammer R. Model for the Correction of Motion-Induced Phase Errors in Multishot Diffusion-Weighted-MRI of the Head: Are Cardiac-Motion-Induced Phase Errors Reproducible From Beat-to-Beat? *Magn Reson Med*. 2012; 68:430–440. [PubMed: 22213138]
46. Johnson CL, Chen DD, Olivero WC, Sutton BP, Georgiadis JG. Effect of Off-Frequency Sampling in Magnetic Resonance Elastography. *Magn Reson Imaging*. 2012; 30:205–212. [PubMed: 22055750]
47. Liu K, Xu Y, Loncar M. Reduced Slab Boundary Artifact in Multi-Slab 3D Fast Spin-Echo Imaging. *Magn Reson Med*. 2000; 44:269–276. [PubMed: 10918326]

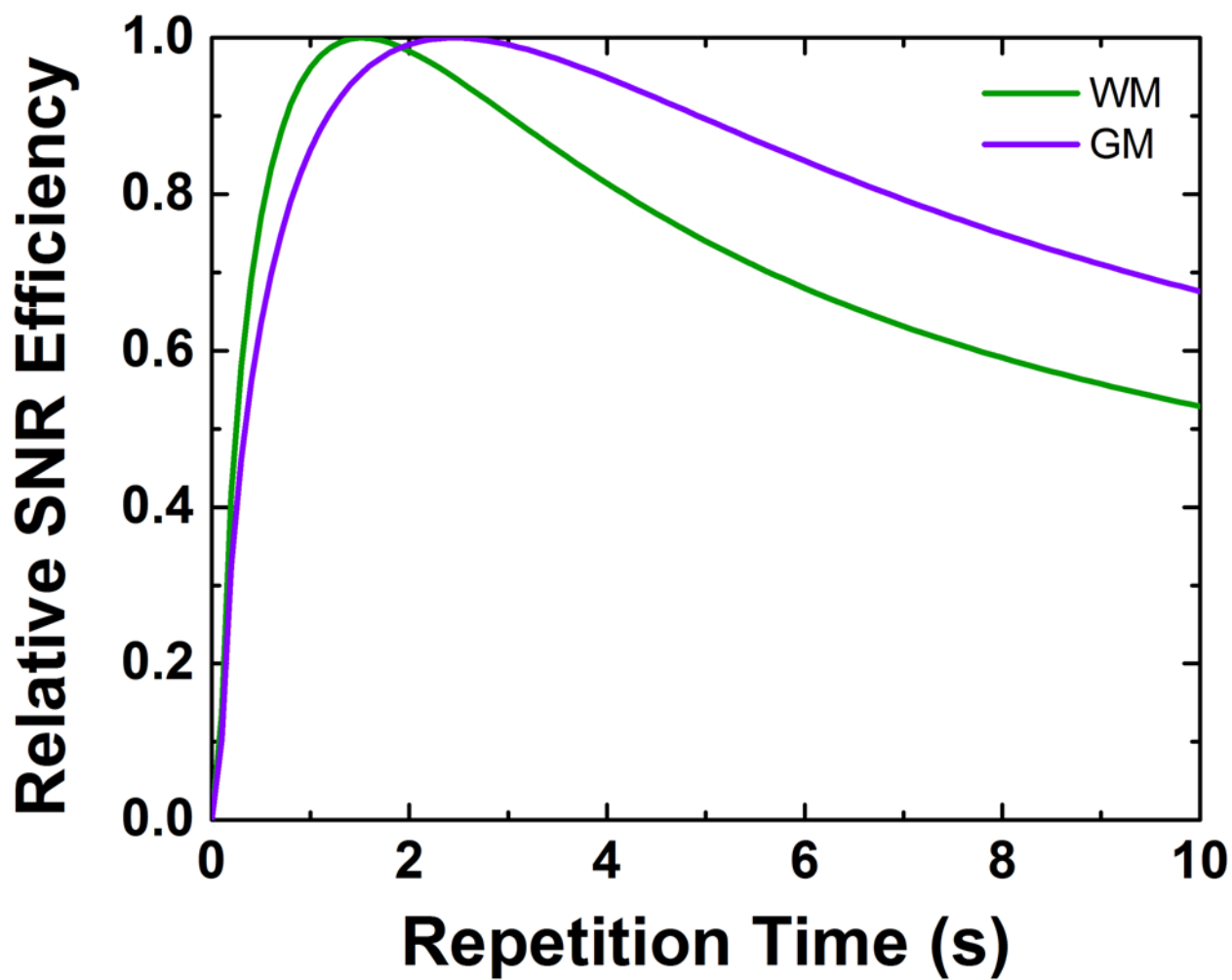


**Fig 1.** Relative SNR efficiency of white and gray matter (green and purple lines, respectively) as a function of TR for a TE of 73 ms. SNR efficiency is defined as the ratio of SNR to the square root of total acquisition time. Tissue  $T_1$ -relaxation times for white and gray matter at 3T (1084 and 1820 ms, respectively) are from Stanisz et al [26].

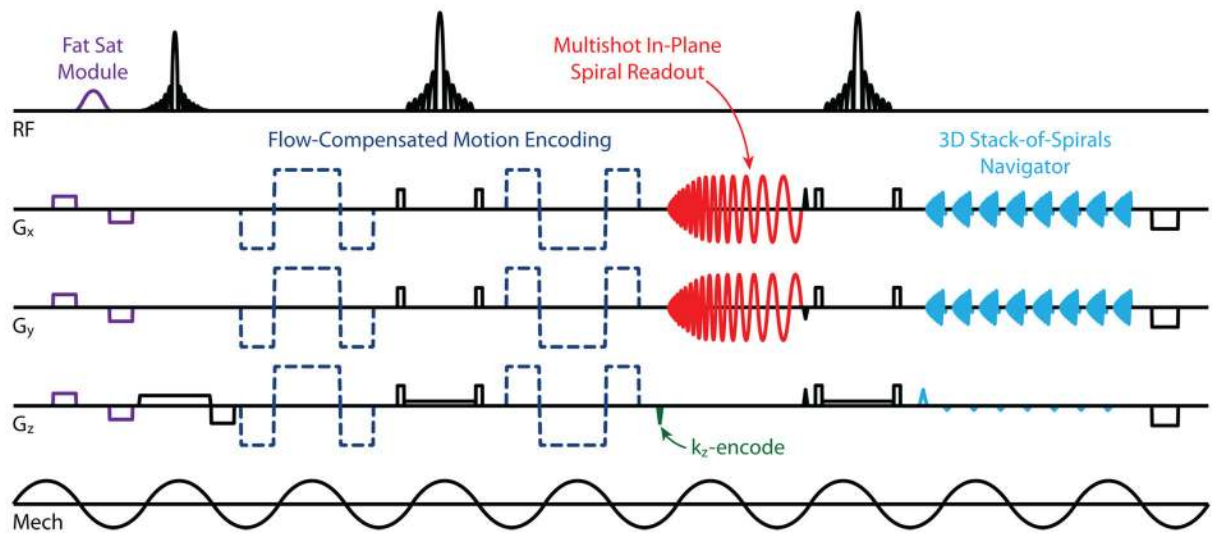


**Fig 2.**

Pulse sequence diagram for proposed 3D multislab, multishot MRE acquisition. Flow-compensated motion encoding gradients are applied on either side of the refocusing pulse and before the in-plane spiral readouts gradients. The 3D  $k$ -space trajectory is a stack-of-spirals with  $k_z$ -encoding blips played before the spiral readout. Following a second refocusing pulse, a low-resolution 3D navigator is acquired as a single-shot stack-of-spirals for motion-induced phase error correction. Each of the ten slabs is excited once per TR of 1.8 s, and multiple TRs are used to encode the slab with a 3D  $k$ -space.

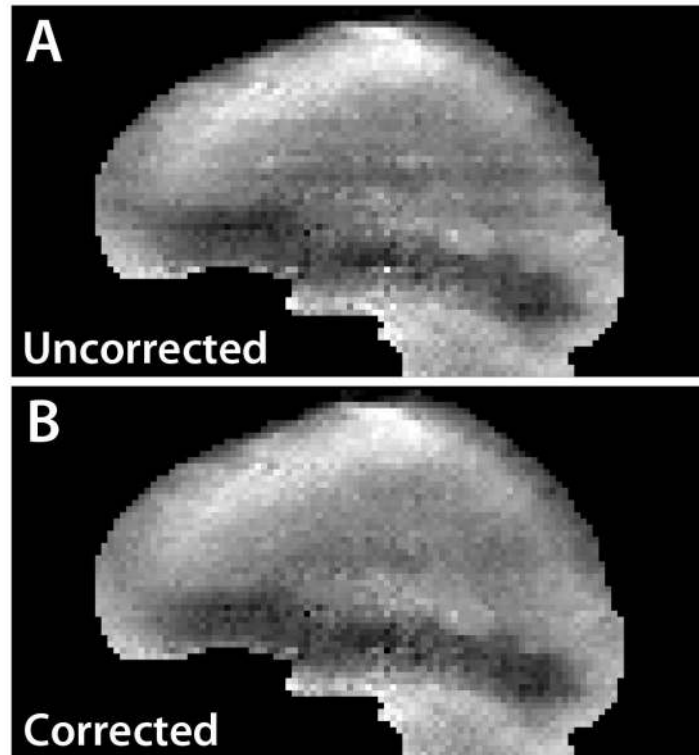


**Fig 3.** Correction for motion-induced phase error improves the quality of phase data. (A) Uncorrected and (B) corrected sagittal reformat of a single time point with  $y$ -encoding after subtraction. The uncorrected dataset shows reduced SNR and slab-to-slab phase inconsistencies, while the smooth phase after correction indicates reduced errors and improved SNR.

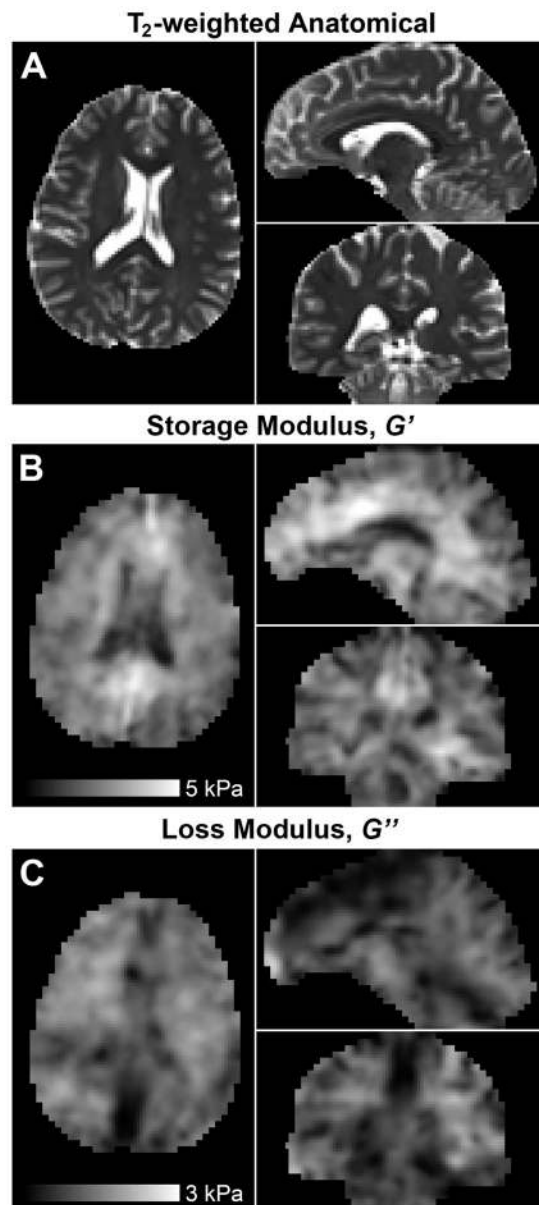


**Fig 4.** Comparison of (A)  $T_2$ -weighted anatomical images with whole-brain maps of mechanical properties, (B) storage modulus and (C) loss modulus, from inversion of MRE displacement data captured with the 3D multislabs, multishot acquisition. Variations in storage modulus seen in axial slices and sagittal and coronal reformats appear to agree well with neuroanatomy. Visible features include cortical sulci, lateral and fourth ventricles, softer cerebellum, and stiff brainstem. Note that differences in edge profiles are due to data masking required by the finite element meshing process of NLI.



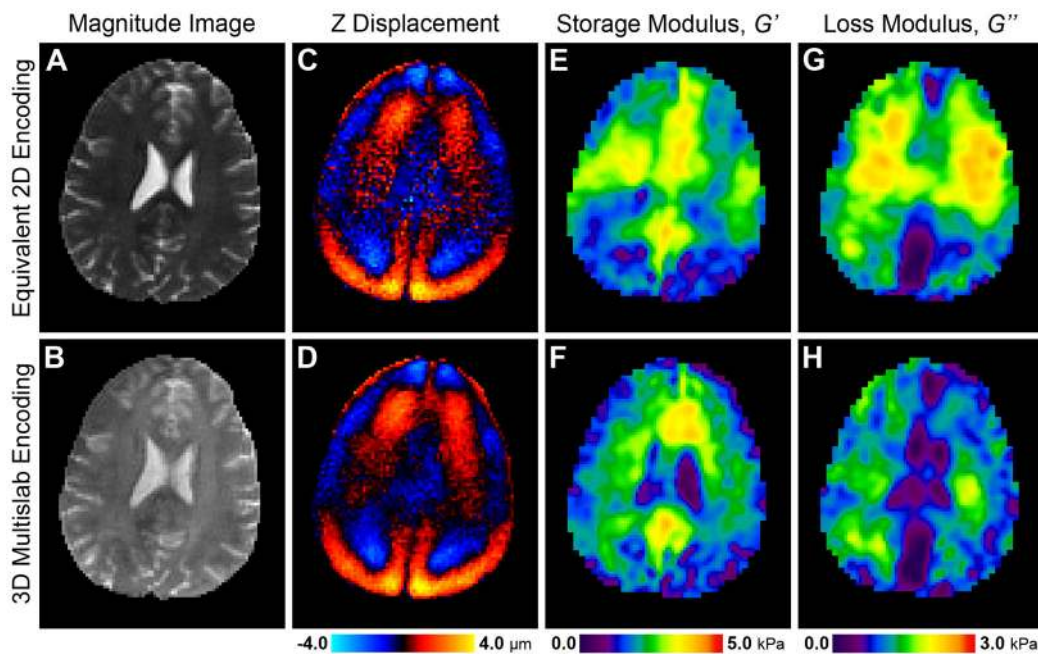


**Fig 5.**

Comparison of a single slice of MRE data captured using (top row) an equivalent 2D acquisition for comparison with (bottom row) the 3D multislab acquisition on the same subject in the same imaging session: (A/B) magnitude image from MRE acquisitions; (C/D) corresponding captured  $z$ -displacements; (E/F) storage modulus property maps; and (G/H) loss modulus property maps. The data acquired in 2D is much noisier and has an OSS-SNR value below the minimum needed for inversion. The excessive noise of the 2D acquisition produces property maps lacking the fine-scale features of the maps calculated from 3D multislab displacement data, most noticeably the lateral ventricles. Note the contrast difference between magnitude images is due to the different TR of the acquisitions.

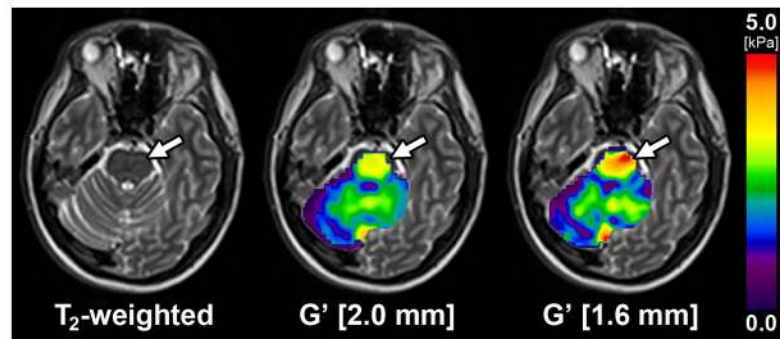


**Fig 6.**

Storage modulus maps of the brainstem and cerebellum calculated from data with  $2.0 \times 2.0 \times 2.0 \text{ mm}^3$  and  $1.6 \times 1.6 \times 1.6 \text{ mm}^3$  isotropic spatial voxel sizes after co-registration to the  $T_2$ -weighted anatomical images. While the property distributions in the cerebellum appear very similar between the two resolutions, with somewhat more detail available from the 1.6 mm data, the brainstem appears as stiffer at higher resolution. The calculated average  $G'$  of the brainstem is 3.01 kPa from 2.0 mm data, and 3.57 kPa from 1.6 mm data.

Average storage and loss moduli for different brain tissue types of the same subject estimated from MRE acquisitions with 2.0 mm and 1.6 mm isotropic spatial resolutions. Standard deviations describe the variation in property across the region mask.

**Table 1**

Property	Storage Modulus, $G'$ [kPa]			Loss Modulus, $G''$ [kPa]		
	2.0 mm	1.6 mm	$d$	2.0 mm	1.6 mm	$d$
Resolution Cerebrum	WM	2.57 ± 0.73	0.04	1.36 ± 0.41	1.35 ± 0.39	0.03
	GM	2.16 ± 0.75	0.07	0.99 ± 0.45	0.99 ± 0.45	0.01
Cerebellum	WM	2.18 ± 0.46	0.04	0.94 ± 0.24	0.97 ± 0.24	0.12
	GM	1.91 ± 0.53	0.19	0.67 ± 0.22	0.63 ± 0.26	0.17
Brainstem		3.01 ± 0.56	0.92 (*)	1.28 ± 0.15	1.11 ± 0.15	1.09 (*)

Effect size, calculated as Cohen's  $d$ , is presented as a measure of the magnitude of the difference in properties based on resolution;

(\*) indicates a large effect size according Cohen ( $\geq 0.8$ ) [40].